Evaluation of 4′-[Methyl-^{11}C]Thiothymidine in a Rodent Tumor and Inflammation Model

Jun Toyohara[1], Philip H. Elsinga[2], Kiichi Ishiwata[1], Jurgen W.A. Sijbesma[2], Rudi A.J.O. Dierckx[2], and Aren van Waarde[2]

[1]Positron Medical Center, Tokyo Metropolitan Institute of Gerontology, Tokyo, Japan; and [2]Nuclear Medicine and Molecular Imaging, University Medical Center Groningen, University of Groningen, Groningen, The Netherlands

4′-[methyl-^{11}C]thiothymidine ([11]C-4DST) is a novel radiopharmaceutical that can be used for tumor imaging because of its rapid incorporation into DNA as a substrate for DNA synthesis. The in vivo stability of [11]C-4DST is much greater than that of natural thymidine, because of the presence of a sulfur atom in the 4′-position. Here, we evaluated the tissue kinetics and biodistribution of [11]C-4DST in a rodent tumor and acute sterile inflammation model in comparison with the previously published biodistribution data of 3′-deoxy-3′-^{18}F-fluorothymidine (^{18}F-FLT), ^{18}F-FDG, ^{11}C-choline, ^{11}C-methionine, and 2 σ-receptor ligands in the same animal model. **Methods:** C6 tumor cells were implanted subcutaneously into the right shoulder and turpentine (0.1 mL) was injected intramuscularly into the left hind leg of male Wistar rats 11 d and 24 h, respectively, before the scanning day. The animals were anesthetized with isoflurane, and [11]C-4DST (20–50 MBq) was injected intravenously. A dynamic PET scan was performed for 60 min with either the shoulder or hind leg region in the field of view. The animals were sacrificed, and a biodistribution study was performed. **Results:** [11]C-4DST showed the highest tumor uptake (standardized uptake value, 4.93) of all radiopharmaceuticals tested. Its tumor-to-muscle concentration ratio (12.7) was similar to that of ^{18}F-FDG (13.2). The selectivity of [11]C-4DST for tumor as compared with acute inflammation was high (37.7), comparable to that of the σ-ligand ^{18}F-FE-SA5845 and much higher than that of ^{18}F-FDG (3.5). Rapidly proliferating tissues (tumor and bone marrow) showed a steadily increasing uptake. In inflamed muscle, [11]C-4DST showed relatively rapid washout, and tracer concentrations in inflamed and noninflamed muscle were not significantly different at intervals greater than 40 min. Competition of endogenous thymidine for [11]C-4DST uptake in target tissues was negligible, in contrast to competition for ^{18}F-FLT uptake. Thus, pretreatment of animals with thymidine phosphorylase was not required before PET with [11]C-4DST. **Conclusion:** In our rodent model, [11]C-4DST showed high tumor uptake (sensitivity) and high tumor selectivity. The different kinetics of [11]C-4DST in rapidly proliferating and inflammatory tissue may allow distinction between tumor and acute inflammation in a clinical setting. These promising results for [11]C-4DST warrant further investigation in PET studies in patients with various types of tumors.

The most widely used radiopharmaceutical in clinical oncology is currently ^{18}F-FDG. Although the applications of ^{18}F-FDG PET in tumor detection, staging, and therapy evaluation are rapidly expanding, ^{18}F-FDG uptake is not tumor-specific; various forms of inflammatory lesion also take up ^{18}F-FDG and are a major cause of false-positive results. Histologic confirmation of ^{18}F-FDG–positive lesions is therefore required for many types of tumor (1–3). Macrophages, which invade tumors, especially after therapeutic intervention, can induce high ^{18}F-FDG uptake and can complicate the interpretation of ^{18}F-FDG PET results (4–6). In addition, decreased uptake of ^{18}F-FDG is seen in hyperglycemic patients and can cause false-negative results.

Several lines of evidence suggest that the accumulation of ^{18}F-FDG is based on enhanced glycolysis, which has often been associated with the growth rate and malignancy of tumor cells. However, all living cells require glucose, and high levels of ^{18}F-FDG uptake are observed in highly metabolic inflammatory cells. More specific information on the in vivo status of tumors may be acquired by the use of a radiopharmaceutical that is a proliferation marker, as proliferative activity is one of the key factors of malignant disease. Various approaches toward tumor-specific visualization have been described in the literature, including the use of radiolabeled amino acids (7), nucleosides (8–10), choline (11–13), and various receptor ligands (14–17). Strictly speaking, only labeled nucleosides that are incorporated into DNA are true proliferation markers, but the tissue kinetics of radiopharmaceuticals tracing amino acid transport, membrane metabolism, enzyme activity, or receptor expression can be used as a surrogate marker of cellular proliferation if the activity of such processes is increased in rapidly dividing cells. In recent years, σ-receptor ligands have been proposed as radiotracers for tumor imaging (14). σ-receptors are overexpressed in rapidly proliferating cells, such as tumor cells from rodent and human origin. A radioligand for visualization of σ-receptors with PET could therefore be useful for

detection of primary tumors and their metastases, for non-invasive assessment of tumor proliferation status, and for determination of the σ-receptor occupancy of antineoplastic drugs. The 2 σ-ligands ^{11}C-SA4503 (selective for the σ_1-subtype) and ^{18}F-FE-SA5845 (not selective for a subtype) are well characterized for tumor imaging (18,19).

We have been engaged in studies of cell proliferation imaging based on the DNA incorporation mechanisms of nucleosides in human tumors (20–24). In recent years, we have developed [11]C-4DST as a new candidate for cell proliferation imaging (25–27). Experiments in a rodent model indicated that replacement of the 4′-position oxygen with sulfur prevents cleavage of deoxyribose from the nucleoside by thymidine phosphorylase, thus conferring resistance to degradation, which is advantageous for in vivo imaging (25). This compound was readily incorporated into the DNA in several mouse tumor models. The standardized uptake value (SUV) is closely correlated with the gold standard, that is, incorporation of ^{14}C-thymidine into DNA (26). Very recently, initial clinical trials of [11]C-4DST PET were reported involving an optimized preparation of [11]C-4DST for injection, safety, radiation dosimetry, and initial brain tumor imaging in human subjects (27). The initial findings in a small group of subjects indicated that [11]C-4DST PET is suitable for imaging brain tumors, with acceptable dosimetry and pharmacologic safety at the dose required for adequate PET imaging. Although the short physical half-life of ^{11}C places a significant limitation on commercial distribution and widespread routine clinical use, it has benefits with regard to lower radiation burden, diagnosis using multiple tracers, such as ^{18}F-FDG and ^{11}C-methionine, and repeated scans during the course of therapy. For this reason, there is a significant opportunity for the use of [11]C-4DST in several clinical settings.

To our knowledge, no information is available about the capability of [11]C-4DST to differentiate between malignant and inflammatory cells. Previously, we developed a rodent model in which each animal bears a tumor and also has sterile inflammation (28,29). This model allows assessment of the tumor selectivity of radiopharmaceuticals, each animal serving as its own control. In this study, we compared the tissue kinetics and biodistribution of [11]C-4DST in a rodent model of tumor and sterile inflammation with previously published biodistribution data of 3′-deoxy-3′-^{18}F-fluorothymidine (^{18}F-FLT), ^{18}F-FDG, ^{11}C-choline, ^{11}C-methionine, and 2 σ-receptor ligands in the same established animal model.

MATERIALS AND METHODS

Chemicals

[11]C-4DST was produced by a palladium-mediated Stille cross-coupling reaction of 5-tributylstannyl-4′-thio-2′-deoxyuridine with ^{11}C-methyl iodide (27). The decay-corrected radiochemical yield was 33% ± 16% (based on ^{11}C-methyl iodide), and specific activities were greater than 71 TBq/mmol at the end of synthesis. The product was dissolved in saline, and radiochemical purities were more than 95%.

Animal Model

Relevant details about our animal model (including PET images and histologic findings) were reported previously (28). C6 glioma cells (2×10^6, in a mixture of Matrigel [Becton Dickinson] and Dulbecco minimal essential medium with 5% fetal calf serum) were subcutaneously injected into the right shoulder of young adult male Wistar rats 11 d before tracer injection. Ten days later, 0.1 mL of turpentine was injected intramuscularly into the thigh of the left hind leg, to produce sterile inflammation within 24 h. Turpentine injection is an established model of sterile inflammation (28,30). The animal experiments were performed by licensed investigators in compliance with the Law of Animal Experiments of The Netherlands. The protocol was approved by the Committee on Animal Ethics of the University of Groningen.

Small-Animal PET

Animals were not kept fasting before the PET scan. In most experiments, 2 animals were scanned simultaneously using a Focus 220 microPET camera (Siemens-Concorde). Three animals were scanned dynamically with the tumors in the field of view. Another 3 animals were scanned dynamically with the abdomen in the field of view. The animals were anesthetized with a mixture of isoflurane and air (inhalation anesthesia, 5% ratio during induction, later reduced to < 2%). The rats were under anesthesia before tracer injection. The tracer ([11]C-4DST) was injected through the penile vein (22–51 MBq/0.6–1.2 nmol). A list-mode protocol was used (60 min). Scanning was started during injection of radioactivity in the lower rat; the upper animal was injected 1 min later.

List-mode data were reframed into a dynamic sequence of 1×15, 1×30, 1×45, 3×60, 1×90, 4×120, 1×210, 2×300, 1×450, and 2×600 s frames. The data were reconstructed per time frame using an iterative reconstruction algorithm provided by Siemens (attenuation-weighted 2-dimensional ordered-subset expectation maximization; 4 iterations; 16 subsets; zoom factor, 2). The final datasets consisted of 95 slices, with a slice thickness of 0.8 mm and an in-plane image matrix of 128×128 pixels of size 1×1 mm. Datasets were fully corrected for random coincidences, scatter, and attenuation. A separate transmission scan (duration, 515 s) was acquired for attenuation correction. The scan was made after the emission scan. Images were smoothed with a gaussian filter (1.35 mm in both transverse and axial directions).

Small-Animal PET Data Analysis

Three-dimensional regions of interest (ROIs) were manually drawn around the outside rim of the tumor (thus, necrotic or underperfused areas of the tumor were included in the tumor ROI) and the bone marrow hot spot (head of the left humerus in 3 rats; head of the right femur in the other 3 rats). As tumor and bone marrow had much higher uptake of [11]C-4DST than any other organ in the field of view (with the exception of the kidneys and urinary bladder), it was rather easy to define the tumor and bone marrow rim accurately. Tumor volumes estimated from the PET images corresponded closely to tumor volumes determined by excision. In contrast, because of the small size of ROIs, particularly in the humerus, partial-volume effects will have resulted in underestimation of bone marrow uptake.

In inflamed muscle and control muscle, a 3-dimensional ROI was carefully drawn around the outside rim of the noninflamed hind leg (in the coronal images), starting in the plane closest to the animal bed and proceeding upward until the skeleton was approached. Care was taken not to include the skeleton in the ROIs. As bone marrow had much higher uptake of [11]C-4DST than any other part of the

hind leg, this goal was achieved easily. The right hind leg had a smaller volume than the swollen left hind leg (inflamed thigh). The volumes (mL) for the noninflamed-muscle ROI were about 50% of the entire volume of the inflamed thigh.

Time–activity curves and volumes (mL) for the ROIs were calculated using standard software (AsiPro, version 6.2.5.0; Siemens-Concorde). PET SUVs were calculated using measured body weights and injected doses and assuming a specific gravity of 1 g/mL for tissue.

Biodistribution Studies

The anesthetized animals were sacrificed after the scanning period (75 min after radiotracer injection). Blood was collected, and plasma and cell fraction were obtained from the blood samples by brief centrifugation (5 min at 1,000g).

Normal tissues (cerebellum, cerebral cortex, rest of brain, white adipose tissue, bladder, bone, bone marrow, heart, large intestine, small intestine, kidney, liver, lung, muscle, pancreas, spleen, and submandibularis) were excised. Urine was collected. The complete tumor (0.86 ± 0.79 g) was excised and separated from muscle and skin. Inflamed muscle could be distinguished from surrounding tissue by its pale color and the odor of turpentine. The inflamed region was excised from the affected thigh. All samples were weighed, and the radioactivity was measured using a CompuGamma CS 1282 counter (LKB-Wallac) with application of decay correction. The results were expressed as dimensionless SUVs (dpm measured per gram of tissue/dpm injected per gram of body weight). Tumor-to-plasma and tumor-to-muscle concentration ratios of radioactivity were also calculated.

The previously published biodistribution data of ^{18}F-FLT, ^{18}F-FDG, ^{11}C-choline, ^{11}C-methionine, and 2 σ-receptor ligands (^{11}C-SA4503 and ^{18}F-FE-SA5845) (28,29) were used for comparison with ^{11}C-4DST data.

Statistical Analysis

Differences between the 2 types of lesion were tested for statistical significance using the 2-sided Student t test. One-way ANOVA with Dunnett multiple-comparison testing was used for comparison of each tracer to ^{11}C-4DST. In all analyses, a P value of less than 0.05 was taken to indicate statistical significance. Tumor-to-plasma and tumor-to-muscle ratios of tracer uptake were calculated for each rat. A tumor selectivity index was calculated for each tracer using the following formula: (tumor SUV – muscle SUV)/(inflammation SUV – muscle SUV). This figure represents the tumor-to-inflammation ratio corrected for background activity. In some animals, the SUV of inflammation was smaller than that of muscle. This occurred in several of the study groups, that is, ^{18}F-FLT + phosphorylase, ^{11}C-SA4503, ^{18}F-FE-SA5845, and ^{11}C-4DST. In such animals, no meaningful value for selectivity index could be obtained, as it was an infinite or negative value. Therefore, in this study, selectivity index was calculated from the average SUV in tumor, inflammation, and muscle for each group rather than from SUVs for individual rats.

RESULTS

Small-Animal PET Images

Small-animal PET images acquired after injection of ^{11}C-4DST are presented in Figure 1. High levels of tracer uptake were observed in tumor and bone marrow. Most activity went to the kidneys, urinary bladder, and urine. Brain uptake was negligible. Inflamed muscle and noninflamed muscle showed low levels of uptake, which were not significantly different from background.
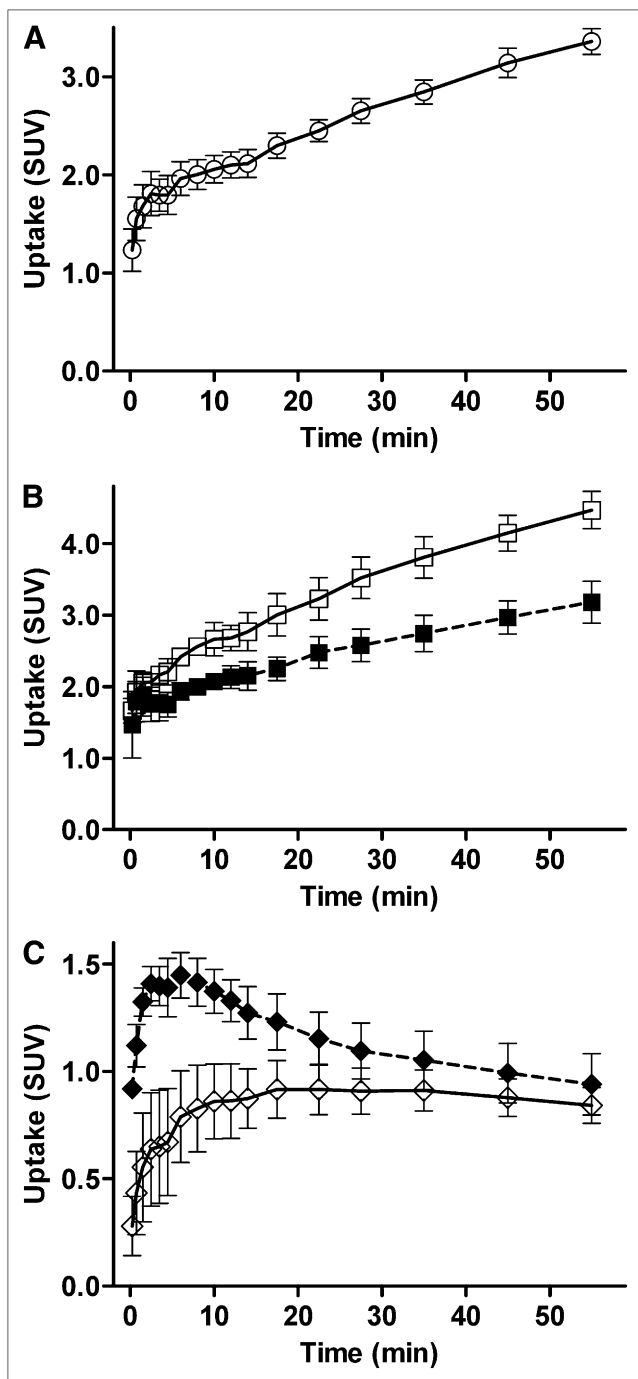
Kinetics of Radioactivity in Tissues

Figure 2 shows the kinetics of ^{11}C-4DST–derived radioactivity (PET SUV in the tissues as a function of time). A steadily increasing level of tracer uptake was observed in rapidly proliferating tissues, such as tumor (Fig. 2A) and bone marrow (Fig. 2B). In muscle (nonproliferating tissue), tracer uptake was low and constant between 20 and 60 min (Fig. 2C). In inflamed muscle, radioactivity peaked at 5–10 min, followed by washout (Fig. 2C). This initial peak may have been due to increased blood flow in the inflamed tissue. At intervals greater than 40 min, tracer uptake levels were not significantly different between inflamed and healthy muscle.

Biodistribution Data

Biodistribution data of ^{11}C, acquired 75 min after injection of ^{11}C-4DST, are presented in Table 1. ^{11}C-4DST showed physiologic high uptake in rapidly proliferating tissues (bone marrow, intestine, spleen, and C6 tumor). A large fraction of the injected dose appeared in urine. Moderate levels of tracer uptake were found in bone, urinary bladder, liver, and kidney. Low uptake of radioactivity was observed in brain, adipose tissue, heart, lung, muscle, pancreas, plasma, red blood cells, submandibular gland, and inflamed muscle. ^{11}C-4DST uptake was 10 times higher in C6 tumor than in plasma,
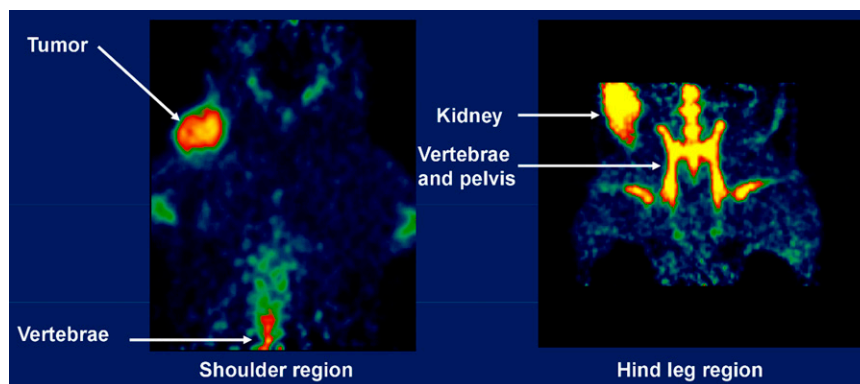
FIGURE 1. Small-animal PET images of rat shoulder region (left) and hind leg region (right) acquired after injection of ^{11}C-4DST (summed frames from 10 min to end of scan).

FIGURE 2. Kinetics of [11]C-4DST–derived radioactivity in C6 tumor (A), marrow (B), and muscle (C). Error bars indicate SD. ○ = C6 tumor; □ = humerus; ■ = femur; ◇ = healthy; ◆ = inflamed.

healthy muscle, and inflamed muscle (Student t test, $P <$ 0.0001). In contrast, [11]C-4DST uptake in inflamed muscle was not different from that in plasma or healthy muscle (Student t test, $P = 0.08$ and 0.72, respectively).

Sensitivity and Selectivity of [11]C-4DST

In our animal model, [11]C-4DST showed the highest level of tumor uptake of all PET tracers tested (Fig. 3A). Tumor-to-plasma ratios of [11]C-4DST (10.0 ± 3.1, $n = 6$) and [11]C-

SA4503 (10.2 ± 2.7, $n = 6$) were similar and much higher than those of other tracers (Fig. 3B). [11]C-4DST (12.7 ± 2.8, $n = 6$) and ^{18}F-FDG (13.2 ± 3.0, $n = 5$) showed much higher tumor-to-muscle contrast than the other tracers (Fig. 3C). [11]C-4DST and ^{18}F-FE-SA5845 showed similar tumor selectivity indices, and the values were the highest among the compounds investigated (Fig. 3D).

DISCUSSION

This study demonstrated the capability of [11]C-4DST to differentiate malignant from inflammatory cells. In addition, the tissue kinetics and biodistribution of [11]C-4DST in a rodent model of tumor and sterile inflammation were compared with previously published biodistribution data of ^{18}F-FLT, ^{18}F-FDG, ^{11}C-choline, ^{11}C-methionine, and 2 σ-receptor ligands in the same established animal model.

In our animal model, [11]C-4DST produced promising results. First, [11]C-4DST showed the highest level of tumor uptake, with high tumor selectivity. Tumor-to-background contrast of [11]C-4DST was similar to that of ^{18}F-FDG. Second, [11]C-4DST showed completely different kinetics in tumor and inflammatory tissues. Third, biodistribution data confirmed that [11]C-4DST is a proliferation marker. These encouraging data support a further clinical pilot study with [11]C-4DST in a range of tumor types.

[11]C-4DST uptake in the tumor increased steadily with time, whereas that in inflamed muscle showed slow exponential clearance after the initial distribution. The kinetics of [11]C-4DST uptake can be expected to be dependent on local blood flow; nucleoside transport across the cell membrane; intracellular metabolism, including nucleoside phosphorylation; and DNA incorporation. Currently, it is unknown which is the rate-limiting step. Preliminary metabolite analysis in mice showed rapid DNA incorporation of [11]C-4DST in proliferating tissues, such as the duodenum and spleen (Supplemental Fig. 1; supplemental materials are available online only at http://jnm.snmjournals.org). The kinetics of DNA incorporation over a 90-min period can generally be modeled by a rectangular hyperbola, with an initial phase of rapid incorporation followed by a plateau of the curve (Supplemental Fig. 1). The plateau level was almost 100%: 99% for the duodenum and 94% for the spleen. The times to reach 50% of the respective plateau levels were rapid: 5.2 min for the duodenum and 7.8 min for the spleen. In contrast, the soluble fraction ([11]C-4DST itself, phosphorylated [11]C-4DST, and some other metabolites) was low over 30 min after injection. These data suggest that the contribution of tissue radioactivity from the DNA incorporation process overshadows all other processes (e.g., blood flow, transport, phosphorylation, and dephosphorylation) at late phases after [11]C-4DST injection. Therefore, in our small-animal PET study, the steady increases in tissue radioactivity may parallel those of DNA incorporation of [11]C-4DST in the late phase (>30 min). Our inflamed muscle model showed acute myositis pathology, including necrotic muscle fibers with massive infiltration of neutrophils, macrophages, and few fibroblasts (28). Although this inflammation model shows high met-

TABLE 1
SUVs at 75 Minutes After Injection

Tissue	11C-4DST (n = 6)
Cerebellum	0.20 ± 0.04
Cortex	0.16 ± 0.03
Rest of brain	0.14 ± 0.02
White adipose tissue	0.13 ± 0.11
Urinary bladder	1.37 ± 0.41
Bone	1.43 ± 0.68
Bone marrow	6.97 ± 1.99
Heart	0.44 ± 0.03
Large intestine	3.40 ± 1.08
Small intestine	7.29 ± 2.73
Kidney	0.90 ± 0.07
Liver	1.10 ± 0.11
Lung	0.60 ± 0.04
Muscle	0.39 ± 0.08
Pancreas	0.45 ± 0.09
Plasma	0.49 ± 0.03
Red blood cells	0.46 ± 0.05
Spleen	2.67 ± 0.66
Submandibularis	0.63 ± 0.06
C6 tumor	4.93 ± 1.42
Inflammation	0.51 ± 0.13
Urine	17.09 ± 6.59

Bone sample contained marrow. Data are mean ± SD.

abolic activity, the mitotic activity of inflammatory cells is low. In contrast, C6 tumor tissues showed many mitotic figures (28). Therefore, the different kinetics in inflammation and tumor tissues may be due to differences in proliferative activity.

Physiologic accumulation of 11C-4DST to levels greater than those in plasma was observed in C6 tumors, bone, bone marrow, the large and small intestine, and the spleen (Table 1).

Many of these organs contain rapidly dividing tissue (malignant cells in the tumor, bone marrow in the skeleton, mucosa in the intestine). Thus, 11C-4DST behaved as a tracer of cellular proliferation. This finding is in good accordance with a recent report suggesting a significant correlation between SUVs of 11C-4DST and proliferative activity of lung tumor lesions (31).

In the present study, 11C-4DST was administered directly to the animals with no phosphorylase pretreatment. In contrast to 18F-FLT, competition of endogenous thymidine for 11C-4DST uptake appeared negligible. Thus, intravenous infusion of thymidine phosphorylase was not required before PET with 11C-4DST. This makes 11C-4-DST much easier to apply than 18F-FLT for therapy monitoring in animal tumor models. Therapy monitoring studies require a high throughput and longitudinal sequential imaging of each animal. As thymidine phosphorylase is supplied in potassium phosphate buffer, a slow rate of infusion was needed in our previous studies on 18F-FLT to avoid myocardial arrest (28). The application of thymidine phosphorylase is impossible in longitudinal studies, as the foreign (bacterial) protein may trigger a response from the immune system of animals, and secondary or tertiary infusions will have a smaller catalytic effect than the initial infusion. Moreover, there is a serious risk of premature loss of animals by cardiac arrest. Fortunately, time-consuming and laborious thymidine phosphorylase pretreatments are not required for small-animal PET scans with 11C-4DST. Furthermore, local thymidine concentrations can be increased by cell killing during the course of therapeutic interventions. Because thymidine competes with 18F-FLT for uptake and trapping in tumor cells, changes in endogenous thymidine may also obscure the therapeutic effect in 18F-FLT imaging. Endogenous thymidine may compete with nucleoside tracers for the active site of nucleoside

FIGURE 3. C6 tumor uptake (SUV), target-to-nontarget ratio, and selectivity index (tumor-to-inflammation ratio corrected for background in normal muscle). Data are plotted as mean ± SD. No SD for selectivity index can be given because, in some animals, tracer uptake in inflamed muscle was equivalent to that in contralateral healthy muscle. 4DST = 11C-4DST (n = 6); CHOL = 11C-choline (n = 4); FDG = 18F-FDG (n = 5); FESA = 18F-FE-SA5845 (n = 6); FLT = 18F-FLT (n = 3); FLT + TP = 18F-FLT + phosphorylase (n = 5); MET = 11C-methionine (n = 4); SA = 11C-SA4503 (n = 6). Original data of CHOL, FDG, FESA, FLT, FLT + TP, MET, and SA are from previous reports (28,29).
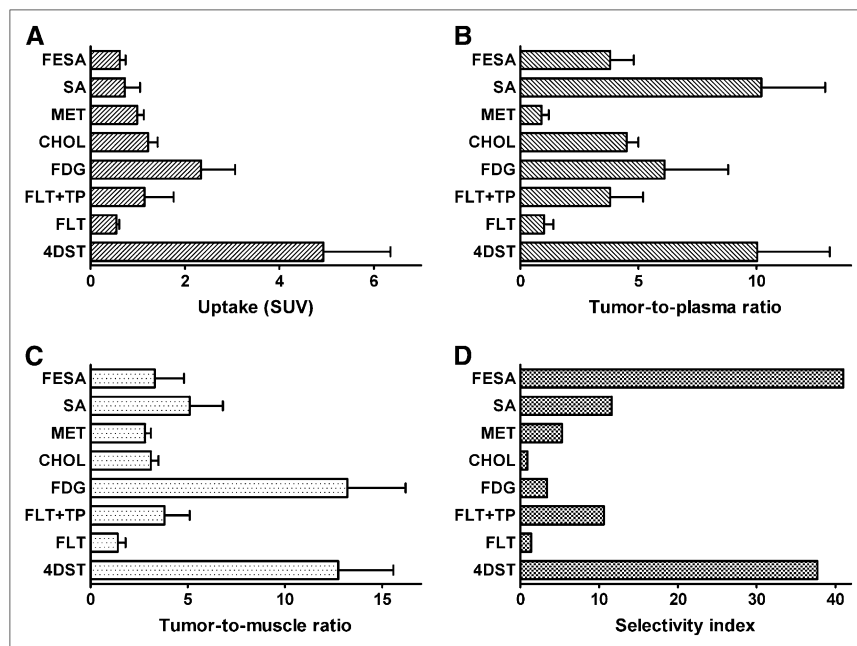
carriers in cell membranes and also for the active site of the trapping enzyme, thymidine kinase 1. The difference between [11]C-4DST and ^{18}F-FLT may be due to distinct affinities or subtype selectivities of the 2 tracers toward nucleoside transporters and thymidine kinase.

Although the usefulness of [11]C-4DST for differentiating between malignant tumors and inflammation was indicated in our experimental model, our study had an important limitation. Turpentine-treated muscle was scanned in the acute phase of inflammation without any contribution of proliferative inflammatory cells. In contrast, chronic inflammatory granulomatous lesions include a Ki-67–positive (6.3%) lymphocyte fraction (32). Indeed, a patient with granulomas showed increased ^{18}F-FLT uptake after radiation and chemotherapy (33). A patient with nonspecific interstitial pneumonia had false-positive ^{18}F-FLT findings (Ki-67 index, 15%) (34). Inflammatory lung diseases are accompanied by lymphocyte infiltration and involve growth factors that enhance the proliferation of lymphocytes (35). As [11]C-4DST is a proliferation marker, [11]C-4DST may accumulate as ^{18}F-FLT does in chronic granulomatous lesions with proliferative inflammation. To confirm [11]C-4DST selectivity, further experimental studies with chronic inflammation models will be needed. In addition, we have used previously published data of other tracers in the same tumor model for comparison purposes. Although the previous experiments were performed in the same laboratory and on the same rodent strain, there is a long interval between previous studies and the current one. Ideally, simultaneous studies are needed for a more direct comparison.

CONCLUSION

[11]C-4DST showed the best characteristics among the tracers evaluated, combining high tumor uptake (sensitivity) with tumor selectivity in our established rodent model. The completely different kinetics of [11]C-4DST in rapidly proliferating tissues and inflamed muscle may allow distinction between tumor and inflammation. The highly promising results for [11]C-4DST warrant further PET studies in patients with various types of tumor. Further extensive clinical trials with [11]C-4DST PET are required.

DISCLOSURE STATEMENT

The costs of publication of this article were defrayed in part by the payment of page charges. Therefore, and solely to indicate this fact, this article is hereby marked "advertisement" in accordance with 18 USC section 1734.

REFERENCES

1. Lorenzen J, de Wit M, Buchert R, Igel B, Bohuslavizik KH. Granulation tissue: pitfall in therapy control with F-18-FDG PET after chemotherapy. *Nuklearmedizin.* 1999;38:333–336.
2. Shreve PD, Anzai Y, Wahl RL. Pitfalls in oncologic diagnosis with FDG PET imaging: physiologic and benign variants. *Radiographics.* 1999;19:61–77.
3. Strauss LG. Fluorine-18 deoxyglucose and false-positive results: a major problem in the diagnostic oncological patients. *Eur J Nucl Med.* 1996;23:1409–1415.
4. Kaim AH, Weber B, Kurrer MO, Gottschalk J, von Schulthess GK, Buck A. Autoradiographic quantification of ^{18}F-FDG uptake in experimental soft-tissue abscesses in rats. *Radiology.* 2002;223:446–451.
5. Kubota R, Kubota K, Yamada S, Tada M, Ido T, Tamahashi N. Microautoradiographic study for the differentiation of intratumoral macrophages, granulation tissues and cancer cells by the dynamics of fluorine-18-fluorodeoxyglucose uptake. *J Nucl Med.* 1994;35:104–112.
6. Kubota R, Yamada S, Kubota K, Ishiwata K, Tamahashi N, Ido T. Intratumoral distribution of fluorine-18-fluorodeoxyglucose in vivo: high accumulation in macrophages and granulation tissues studied by microautoradiography. *J Nucl Med.* 1992;33:1972–1980.
7. Jager PL, Vaalburg W, Prium J, et al. Radiolabeled amino acids: basic aspects and clinical applications in oncology. *J Nucl Med.* 2001;42:432–445.
8. Toyohara J, Fujibayashi Y. Trends in nucleoside tracer for PET imaging of cell proliferation. *Nucl Med Biol.* 2003;30:681–685.
9. Bading JR, Shields AF. Imaging of cell proliferation: status and prospects. *J Nucl Med.* 2008;49(suppl):64S–80S.
10. Been LB, Suurmeijer AJ, Cobben DC, et al. [18F]FLT-PET in oncology: current status and opportunities. *Eur J Nucl Med Mol Imaging.* 2004;31:1659–1672.
11. Shinoura N, Nishijima M, Hara T, et al. Brain tumors: detection with C-11 choline PET. *Radiology.* 1997;202:497–503.
12. Hara T, Kosaka N, Kishi H. PET imaging of prostate cancer using carbon-11 choline. *J Nucl Med.* 1998;39:990–995.
13. de Jong IJ, Prium J, Elsinga PH, et al. Visualization of prostate cancer with ^{11}C-choline positron emission tomography. *Eur Urol.* 2002;42:18–23.
14. van Waarde A, Rybczynska AA, Ramakrishnan N, Ishiwata K, Elsinga PH. Sigma receptors in oncology: therapeutic and diagnostic applications of sigma ligands. *Curr Pharm Des.* 2010;16:3519–3537.
15. Van de Wiele C, Boersma H, Dierckx RA, De Spiegeleer B, van Waarde A, Elsinga PH. Growth factor/peptide receptor imaging for the development of targeted therapy in oncology. *Curr Pharm Des.* 2008;14:3340–3347.
16. Koopmans KP, Neels ON, Kema IP, et al. Molecular imaging in neuroendocrine tumors: molecular uptake mechanisms and clinical results. *Crit Rev Oncol Hematol.* 2009;71:199–213.
17. de Vries EF, Rots MG, Hospers GA. Nuclear imaging of hormonal receptor status in breast cancer: a tool for guiding endocrine treatment and drug development. *Curr Cancer Drug Targets.* 2007;7:510–519.
18. Kawamura K, Kubota K, Kobayashi T, et al. Evaluation of [^{11}C]SA5845 and [^{11}C] SA4503 for imaging of sigma receptors in tumors by animal PET. *Ann Nucl Med.* 2005;19:701–709.
19. van Waarde A, Buursma AR, Hospers GA, et al. Tumor imaging with 2 σ-receptor ligands, ^{18}F-FE-SA5845 and ^{11}C-SA4503: a feasibility study. *J Nucl Med.* 2004;45:1939–1945.
20. Toyohara J, Hayashi A, Sato M, et al. Rationale of 5-[^{125}I]iodo-4′-thio-2′-deoxyuridine as a potential iodinated proliferation marker. *J Nucl Med.* 2002;43:1218–1226.
21. Toyohara J, Gogami A, Hayashi A, Yonekura Y, Fujibayashi Y. Pharmacokinetics and metabolism of 5-^{125}I-iodo-4′-thio-2′-deoxyurieine in rodents. *J Nucl Med.* 2003;44:1671–1676.
22. Toyohara J, Hayashi A, Gogami A, et al. Development of radioiodinated nucleoside analogs for imaging tissue proliferation: comparisons of six 5-iodonucleosides. *Nucl Med Biol.* 2003;30:687–696.
23. Toyohara J, Hayashi A, Gogami A, et al. Alkyl-fluorinated thymidine derivatives for imaging cell proliferation—I. The in vitro evaluation of some alkyl-fluorinated thymidine derivatives. *Nucl Med Biol.* 2006;33:751–764.
24. Toyohara J, Hayashi A, Gogami A, Fujibayashi Y. Alkyl-fluorinated thymidine derivatives for imaging cell proliferation—II. Synthesis and evaluation of N^3-(2-[^{18}F]fluoroethyl)-thymidine. *Nucl Med Biol.* 2006;33:765–772.
25. Toyohara J, Kumata K, Fukushi K, Irie T, Suzuki K. Evaluation of [methyl-^{14}C]4′-thiothymidine for *in vivo* DNA synthesis imaging. *J Nucl Med.* 2006;47:1717–1722.
26. Toyohara J, Okada M, Toramatsu C, Suzuki K, Irie T. Feasibility studies of 4′-[methyl-^{11}C]thiothymidine as a tumor proliferation imaging agent in mice. *Nucl Med Biol.* 2008;35:67–74.
27. Toyohara J, Nariai T, Sakata M, et al. Whole-body distribution and brain tumor imaging with [11]C-4DST: a pilot study. *J Nucl Med.* 2011;52:1322–1328.

28. van Waarde A, Cobben DCP, Suurmeijer AJH, et al. Selectivity of ^{18}F-FLT and ^{18}F-FDG for differentiating tumor from inflammation in a rodent model. *J Nucl Med.* 2004;45:695–700.

29. van Waarde A, Jager PL, Ishiwata K, Dierckx RA, Elsinga PH. Comparison of sigma-ligands and metabolic PET tracers for differentiating tumor from inflammation. *J Nucl Med.* 2006;47:150–154.

30. Yamada S, Kubota K, Kubota R, Ido T, Tamahashi N. High accumulation of fluorine-18-fluorodeoxyglucose in turpentine-induced inflammatory tissue. *J Nucl Med.* 1995;36:1301–1306.

31. Minamimoto R, Kubota K, Morooka M, et al. DNA synthesis imaging of non-small-cell lung cancer using a new PET tracer [^{11}C]4DST [abstract]. *J Nucl Med.* 2011;52 (suppl):425P.

32. Zhao S, Kuge Y, Kohanawa M, et al. Usefulness of ^{11}C-methionine for differentiating tumors from granulomas in experimental rat models: a comparison with ^{18}F-FDG and ^{18}F-FLT. *J Nucl Med.* 2008;49:135–141.

33. Saga T, Kawashima H, Araki N, et al. Evaluation of primary brain tumors with FLT-PET: usefulness and limitations. *Clin Nucl Med.* 2006;31:774–780.

34. Yap CS, Czernin J, Fishbein MC, et al. Evaluation of thoracic tumor with ^{18}F-fluorothymidine and ^{18}F-fluorodeoxyglucose-positron emission tomography. *Chest.* 2006;129:393–401.

35. Drent M, du Bois RM, Poletti V. Recent advances in the diagnosis and management of nonspecific interstitial pneumonia. *Curr Opin Pulm Med.* 2003;9:411–417.